Low temperature thermally reduced graphene oxide directly on Ni – Foam using atmospheric pressure – chemical vapour deposition for high performance supercapacitor application

Vusani M. Maphiri, Daba T. Bakhoum, Samba Sarr, Ndeye F. Sylla, Gift Rutavi, Ncholu Manyala*

Department of Physics, Institute of Applied Materials, SARChI Chair in Carbon Technology and Materials, University of Pretoria, Pretoria 0028, South Africa

*Corresponding author email: ncholu.manyala@up.ac.za, Tel.: + (27)12 420 3549 Fax: + (27)12 420 2516

Abstract.

A binder free approach was use to prepare thermally reduced graphene oxide (TRGO) at 200 ℃ directly on Ni – Foam (NF) (current collector) via atmospheric pressure – chemical vapour deposition (AP – CVD) and used as a positive electrode for supercapacitor application. The TRGO/NF electrode preparation method is simpler, quicker, cheaper and more effective compared to other method. The half-cell electrochemical performances in 6 M KOH showed a maximum specific capacity of 52.64 mA h g^{-1} at 0.5 A g^{-1}. The device: TRGO/NF// PAC showed a specific energy and power of 18.72 W h kg^{-1} and 547.52 W kg^{-1} respectively at 1 A g^{-1}; and 14.10 W h kg^{-1} and 2.5 kW kg^{-1} respectively at 5 A g^{-1}. The high coulombic efficiency (99.9 %) and capacitance retention (70 %) indicate outstanding stability. These results represent a significant progress in the fabrication of binder and conductive enhancement free positive electrode for electrochemical energy storage devices.

Keywords: Thermally reduced; Energy storage; Chemical Vapour Deposition; Graphene Oxide; Ni – Foam; Binder – free supercapacitor

1. Introduction

Recently researchers are paying a great attention in the development of alternative energy storage and conversion devices such as supercapacitors (SCs) and batteries, to help in combating energy related problems of environmental pollution, depletion of fossil fuels, efficient mobile (potable) energy source and many more [1–12]. SCs devices are unique and attractive due to their high power density, wide range of operation temperature, fast charge and discharge rates and long cycle life [13–16]. These devices bridge the gap between high power and low energy convention capacitors and low power and high energy batteries. SCs can be classified according to the energy storage mechanism which either involves electric double layer capacitors (EDLCs) or pseudocapacitors. EDLCs store their energy through surface charge adsorption related to the electrical double layer formation. Thus, the electrode materials are mainly characterized by large specific surface areas, being mostly carbon materials such as activated carbon, carbon onions and reduced graphene oxide. Meanwhile, pseudocapacitors store energy based on Faradaic processes which depends on the operational voltage. Most pseudocapacitors material are from the transition metal compounds like oxides, hydroxides or sulphides, and conductive polymers, such as polyaniline, polypyrrol, and poly (3,4-ethylenedioxythiophene). Carbon materials such as graphene suffer from poor electrochemical performance due to the undesirable ion diffusion inside its internal surface and only electrical layer absorption mechanism occurs [17,18].

Recently, efforts have been devoted in developing thermally reduced graphene oxide (TRGO) materials suitable for high-performance supercapacitor application. TRGO has been prepared via a combinations of chemical oxidization of carbon material like graphite using Hummer's method and the thermal reduction process which is simple, quick, cheap, effective, safe and easily scalable than other reduction methods such as bio reduction [19], chemical [20,21], photoreduction [22,23] and mechanochemical [24], [16,25,26]. Zhao et al. [16] reported the increased performance of graphene oxide thermally reduced at low temperature using a horizontal tube furnace under nitrogen. The sample reduced at 200 ℃ had the highest capacitance of 260.5 Fg^{-1} due to the presence of functional groups on the external surface serving as a passage for ions to the internal surface. These functional groups were also reported to facilitate fast redox processes leading to pseudocapacitance behaviour and also

enhancing the charge storage capabilities [17,27–29]. Graphene has been coated on different substrates via various method such as chemical vapour deposition, slurry paste, spin coating, spray coating, dip coating and electrophoretic deposition [28,30,31]. Among them, slurry paste is the simplest method to deposited GO nano sheets on Ni-Foam (NF). This method is well developed, quick, cheap, environmentally friendly as it does not require any sophisticated and expensive equipment. This method has been widely used to prepare activated carbon and metal compounds on NF [14,16,32–34]. Ramadoss et al. [28] reported TRGO coated fabric supercapacitor prepared via GO dip coating, followed by thermal treatment at 160 ℃ in Ar for 2 hours. The fabricated symmetric supercapacitor yielded a specific energy and power of 5.8 W h Kg^{-1} and 27.7 kW kg^{-1}, respectively, at a current density of 0.1 mA cm^{-2}. However, TRGO/NF as an electrode for supercapacitor applications prepared by slurry paste followed by thermal treatment has never been reported.

In this study, the GO was reduced directly on NF (current collector) at 200 ℃ eliminating the need for binders such as poly(vinylidenedifluoride) (PVDF) and conductive additives like carbon acetylene black (CAB) which tampers with the overall electrochemical performance of the material under study. This fabrication was only possible due to the restacking ability of reduced graphene oxide which occurs without the presences of binding agents, which formed a macroscopic assemble structure .i.e. graphene film around three dimensional (3D) NF structure [35,36]. This is not possible within other non-two dimensional carbon allotropes and carbon based nanocomposite material such as carbon nanotube, activated carbon and iron carbide [37–42]. Inorganic active material such as Nickel subsulfide (Ni_3S_2) and Zinc sulphide have been successful deposited on NF without any additives [43,44]. Studies have been under taken to illustrate the effects of the binders [33,34] and conductive additives [45]. Zhu et al. [33] reported the effects of binders; Nafion, Polytetrafluorethylene (PTFE) and PVDF while using carbon nanotube as a conductive agent. The PTFE sample had higher capacitance retention of 90.8 % while PVDF and Naflon had 79.7 and 87 %, respectively. However, Liu et al. [45] reported the enhancement of the electrochemical performance of NiCo-MOF nanosheets by the addition of acetylene black. The sample containing CAB had an increased specific capacitance and a lower solution resistance as compared to the one without CAB. Additive free electrodes have been mostly reported for free standing electrodes [46–48], but Moyseowicz et al. [49] reported a binder free poly(aniline-co-pyrrole)/thermally reduced graphene oxide (PAP/TRGO) composite. The PAP/TRGO//PAP/TRGO device

showed a high specific capacitance of 287 F g^{-1} and good rate capability of 205 F g^{-1} at 20 A g^{-1}. However, this material had a low specific energy of 6.3 W h kg^{-1} and specific power of 100 W kg^{-1} at specific current of 0.2 A g^{-1}. Our prepared device TRGO/NF//PAC showed a better electrochemical performance with specific energy of 18.73 W h kg^{-1} and specific power of 547.52 W kg^{-1} at specific current of 1 A g^{-1}, signifying the readiness of additive free electrode for supercapacitor application. Moreover directly reduced GO on NF without the binder and conductive additives avoids inactive surfaces with conversational binder electrodes and allows for more efficient charge transport. This allows the proper measurement of the material without any influence from additive.

2. Experimental

2.1.Materials

Reagents utilized in this work were analytical grade and used without any further purification. These include raw graphite, sulphuric acid [H_2SO_4 (98%)], potassium permanganate [$KMnO_4$], hydrogen peroxide [H_2O_2 (50%)], ethanol [C_2H_5OH], hydrogen [H_2], Argon [Ar] nickel foam [NF, thickness and areal density of 1.6 mm and 420 g m^{-2}], potassium hydroxide [KOH] pallets and distilled water (DW) at 18.2 MΩ.

2.2. Preparation of GO

The Hummer's method was used to prepare GO in the same manner as reported in our pervious study [30]. Briefly, 2 g of graphite powder was added into cooled 120 ml of H_2SO_4 and stirred using a magnetic stirrer until a homogenous black lump free solution is reached. 6 g of $KMnO_4$ was also added slowly into the cooled homogeneous solution of graphite and H_2SO_4. This mixture was stirred for 180 minutes at a constant heating temperature of 50 ℃. The brownish solution was allowed to cool to room temperature, and then further cooled in an ice bath for an hour. 100 ml of H_2O and 20 ml of H_2O_2 were then added to stop the reaction. The mixture was stirred and left to settle. The suspended liquid was discarded; DW was added to the settled GO mixture and left to re-settle then followed by discarding the DW.

This process was repeated several times to remove contaminants. The GO mixture was centrifuged at 5000 rpm for 5 minutes and dried in an oven at 60 ℃ overnight.

2.3. Preparation of TRGO/NF electrode

Dried GO was mixed with ethanol, then sonicated (approximately, 30 minutes) together with manual stirring until it reached a paste like. The GO paste was then pasted on NF and dried at room temperature. The dimensions of the pasted area on rectangular and circular NF are 1.0 × 1.0 cm^2 and thickness-diameter of 0.2 – 16 mm. The GO/NFs were placed in the atmospheric pressure-chemical vapour deposition (AP-CVD) for thermal reduction. The Ar was allowed to flow at 300 standard cubic centimetres (sccm) throughout the entire reduction process, to avoid oxidation. The following heat settings were used: Heating rate was set to 10 ℃/min until the desired temperature of 200 ℃ was reached; the AP-CVD was kept at that temperature for an hour. After an hour the CVD was moved away from the region with TRGO/NF to allow the electrode to cool down to room temperature. The TRGO/NF electrode preparation is displayed in Fig. 1.

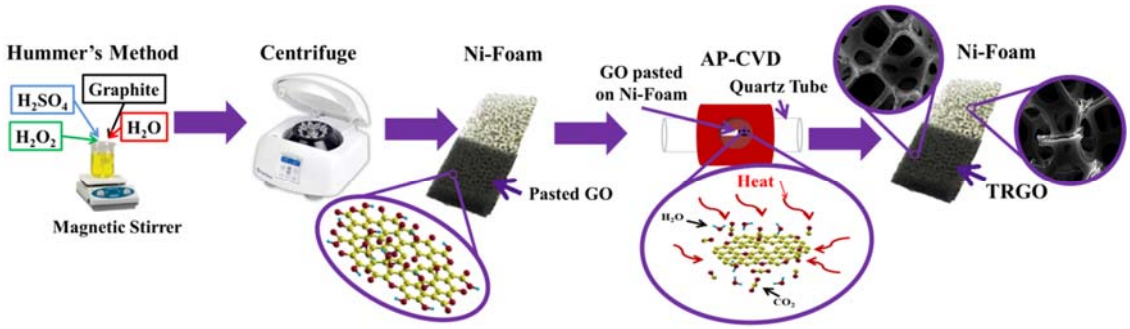

Fig. 1. Schematic of the synthesis route for TRGO/NF electrode

2.4.Characterization

The structural, morphology and compositional characterization were performed using the following: Bruker BV 2D PHASER Best Benchtop X-ray diffraction (XRD) with reflection geometry at 2θ values (15 – 90 °) in a step size of 0.005° using Cu K∝ radiation source (λ = 0.15406 nm) at 50 kV and 30 mA; Bruker Alpha platinum-ATR Fourier transform infrared

spectroscopy (FTIR) at 32 scans in the range of 400 – 4000 cm^{-1}. WITec Raman 300 RAS+ operated using Zeiss objective 10×, 20×, 50× and 100× at a laser of 532 nm and a power of < 0.5 mW (to avoid further GO reduction due to sample heating or damage by the laser generated heat) at a grating of 600 g/mm BLZ = 500 nm. The Raman mapping was performed on a 25 × 25 μm^2 area and 300 by 300 lines per image and point per line at an integration time of 1 second. The optical image of the measured area is displayed on Fig. S1 in the supplementary information. The WITec Project five (Build 5.0.3043, plus version) software was used for data analysis and achieving the Raman mapping images. The morphology and elemental composition was obtained using Zeiss Ultra Plus 55 field emission scanning electron microscope (SEM) operated at 2.0 kV coupled with energy-dispersive X-ray spectroscopy (EDS) at 20 kV. The two and three electrode configurations measurements (cyclic voltammeter (CV), galvanostatic charge-discharge (GCD) and electrochemical impendence spectroscopy (EIS)) were performed using the Bio – Logic VMP-300 (Knoxville TN 37,930, USA) potentiostat monitored by the EC-Lab V11.33 software.

3. Results

3.1.Structural, morphological and compositional characterization

The normalized XRD pattern of graphite, GO, NF and TRGO/NF were measured and displayed in Fig. 2 (a). The obtained XRD pattern were indexed to the Joint Committee on Powder Diffraction Standards (JCPDS) 75 2078, JCPDS 41 1487 and JCPDS 04 0850 for graphite, GO and NF, respectively [50,51]. The precursor (graphite) showed a dominant peak around 2θ = 25 ° corresponding to the (002) plane due to the sp^2 –bonded sheets. The GO show a reflection plane at 2θ = 20 ° corresponding to the (001) indices, a hump labelled peak II has been attributed to amorphous-like carbon comprising of impurities, defects or folding wrinkles [52] and the peak around 2θ = 43 ° is indexed to (100) plane [53]. The interplanar spacing calculated using the Bragg's equation showed 80% increase in the graphite sheet spacing. The interplanar spacing is small in comparison to those reported within Ref [16]. This is due to the 60 ℃ drying temperature which has mostly removed the intercalated H_2O, resulting in a reduction of the interplanar spacing. The pattern of NF showed the diffraction

plane corresponding to the (111), (200) and (220). Similar diffraction peaks were reported on Refs [54–57]. The pattern from TRGO/NF only show peaks from pure NF because the TRGO reduced at 200 ℃ is not highly crystalline and it is of low amount with respect to NF. The FTIR spectra of graphite and GO are displayed in Fig. 2 (b). Note that TRGO/NF sample was not measured due to its form. The graphite shows the absence of notches (i.e. showed a linear spectra) due to the absence of surface functional groups on the graphene sheets, indicating chemical inertness of bulk graphite [58]. On the other hand GO showed the presence of many notches at various wavenumbers such as 3170, 1728, 1606, 1205, and 1044 cm^{-1}. The notch at around 3170 cm^{-1} is due to the stretching of hydroxyl (-OH) group. The dip at 1728 cm^{-1} is attributed to the stretching of carbonyl (-C=O) functional group and the 1606 cm^{-1} corresponds to the stretching vibrations of the un-oxidized graphitic domain, while the 1205 cm^{-1} is due to the epoxy (C-O) group. The alkoxy (C-O) group stretching vibration was attributed to the notch at 1044 cm^{-1}. These results are in line with those reported in literature [32,58,59] and also verifies the increased interplanar distance seen on the XRD in Fig. 2 (a) due to the functional groups on the surface of graphene sheets. The EDS spectra are displayed in Fig. 3 (c) and the inset to the figure shows the zoomed (in the 0 – 1 keV region) spectra of graphite, GO, NF and TRGO/NF, respectively. The EDS spectra show the expected elements; carbon (C), oxygen (O), nickel (Ni) and a traces of sulphur (S) and potassium (K) from the oxidation solution. Graphite is predominately a pure carbon material having a higher carbon content (calculated from peak intensity of carbon to oxygen) of 110. The GO powder has carbon from graphite and oxygen from the functional groups. The calculated carbon content of GO is 2. The TRGO/NF has Ni peaks in addition to those of GO. This is because GO was reduced on NF current collector and has a carbon content of 5. The carbon content increased because of removal of oxygen functional groups due to the thermal reduction. Similar, carbon content has been reported for low temperature TRGO [16,60]. The scanning electron microscopy image of the TRGO/NF is displayed in Fig. 3 (a); while the corresponding EDS mapping are displayed in Fig. 3 (b) – (d) which show a uniform distribution of elements.

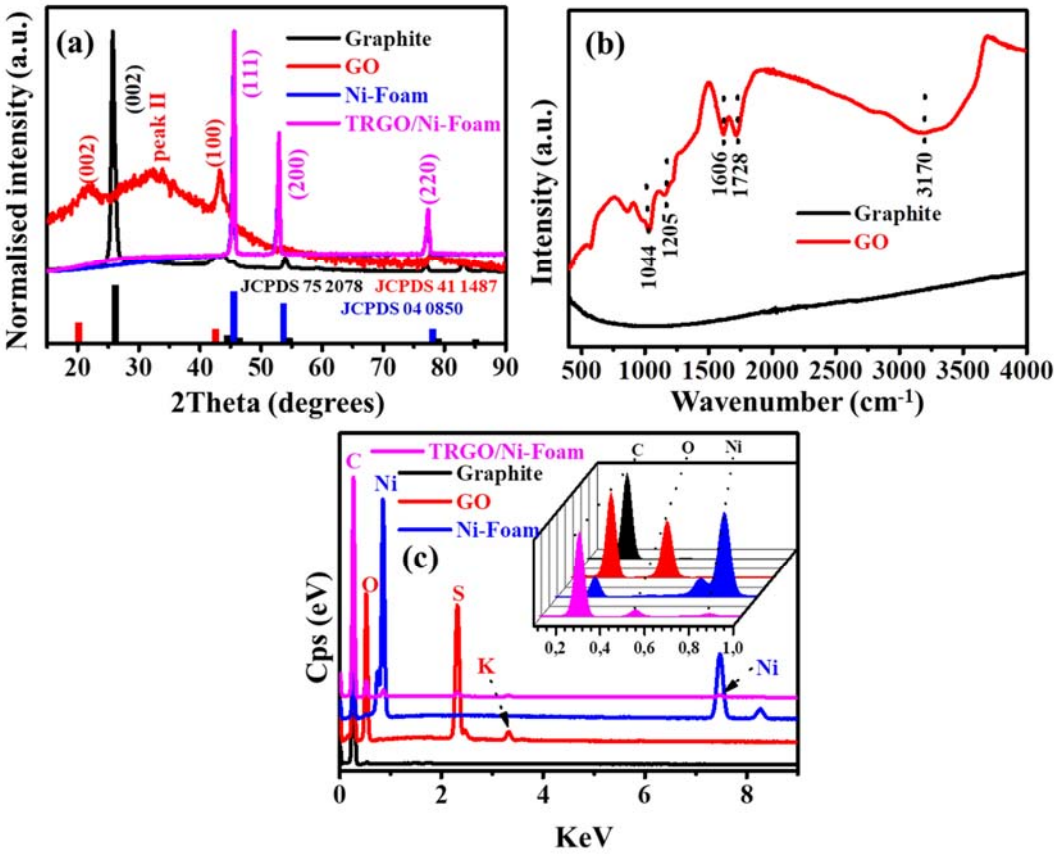

Fig. 2. (a) XRD pattern, (b) FTIR spectra and (c) EDS spectra of Graphite, GO, NF and TRGO/NF.

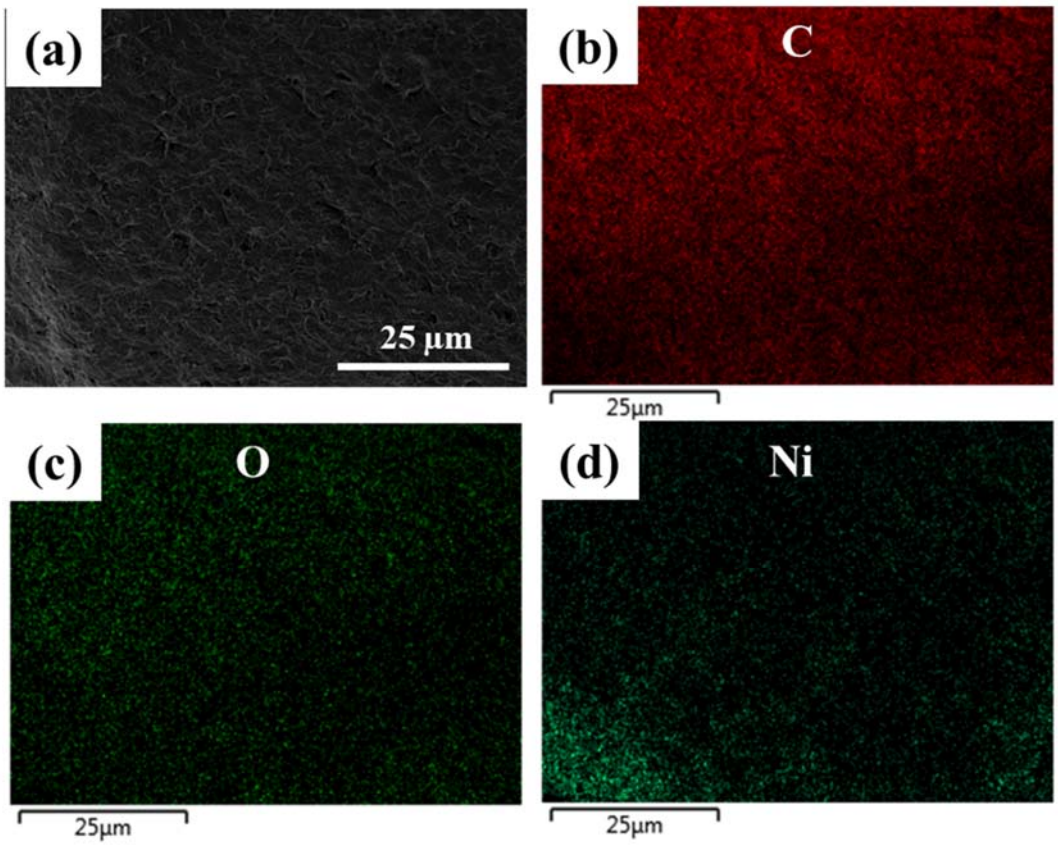

Fig. 3. (a) Scanning electron microscopy image and (b) – (d) the corresponding energy dispersive X-ray maps of C, O and Ni obtained from the TRGO sample.

Raman spectra of graphite, GO and TRGO/NF are displayed in Fig. 4 (a). The graphite sample only shows three peaks at ~ 1337, 1590 and 2694 cm^{-1} corresponding to the D, G and 2D peak, respectively, while the GO and TRGO/NF shows additional second order peaks at around 2964 and 3199 cm^{-1} corresponding to the D + G and 2D' [52,61–63]. The D (defect-induced) peak is related to the A_{1g} breathing mode [64,65], while the G and 2D peaks are attributed to the first and second-order allowed Raman E_{2g} mode, respectively [63]. Furthermore, the D + G and 2D' are attributed to the combination of the G and D modes characteristic for the disturbed graphitic structure and the overtone of the D', respectively [31,52,62]. The de-convoluted one phonon region (800 – 2000 cm^{-1}) of graphite, GO and TRGO/NF are displaced in Fig. 4 (b), (c) and (d), respectively. Only two peaks (D and G) were observed for the graphite and five (D*, D, D'', G and D') for the GO and TRGO/NF. The D* peak is due to the sp^2 - sp^3 bonds at the edges of the network, while this peak has been also attributed to the ionic impurities [66,67]. The D'' peak has been attributed to the

amorphous carbon [66] and D' has been attributed to the disorder – induced phonon mode due to crystal defects i.e. the vacancy corresponding to pentagonal and octagonal rings [62,63,68,69]. The full width at half maximum (FWHM) of the D peak increased due to the high concentration of defects related to the oxidation and the alteration of the basal plane structure of graphene during the thermal reduction [52,62]. The integrated ratio of the D peak over the integrated ratio of the G peak (I_D/I_G) of graphite, GO and TRGO/NF were calculated to be 0.14, 2.63 and 3.09, respectively. Thus, graphite is highly ordered than GO and TRGO/NF due to the destruction of the sp^2 cluster during the oxidation process. Tuinstra – Koenig model [64,70] shows the relationship between I_D/I_G and the average crystallite size L_a (or the average sp^2 cluster) via the Knight equation 1 below [14,52,62,70]:

$$L_a = \frac{C(\lambda)}{I_D/I_G}\ [nm] \qquad \ldots (1)$$

where $C(\lambda)$ is the wavelength-dependent pre-factor estimated using $C(\lambda) \approx C_o + \lambda C_1$, for $400 < \lambda < 700$ nm and $C(\lambda) = 4.96$ nm for $\lambda = 532$ nm, where C_0 and C_1were estimated to be -12.6 nm and 0.033, respectively [64]. The I_D/I_G is the ratio of the intergraded area of the D and G peak from the spectra in Fig. 4 (b) – (d). The L_a for graphite, GO and TRGO/NF were calculated to be 35.43, 1.89 and 1.61 nm, respectively. More like I_D/I_G, the L_a decrease from graphite to GO due to the disruption of the sp^2 cluster during oxidation [62] and the thermal reduction. The degree of amorphous carbon was estimated by the intergraded area of D" and G peaks ratio ($I_{D"}/I_G$). The $I_{D"}/I_G$ of GO is 0.40 and TRGO/NF is 0.82, and has increased due to the removal of the carbon atom together with the oxygen-functional groups upon reduction. Our previous results [14,71] showed the influence of the amorphous carbon on the electrochemical performance.

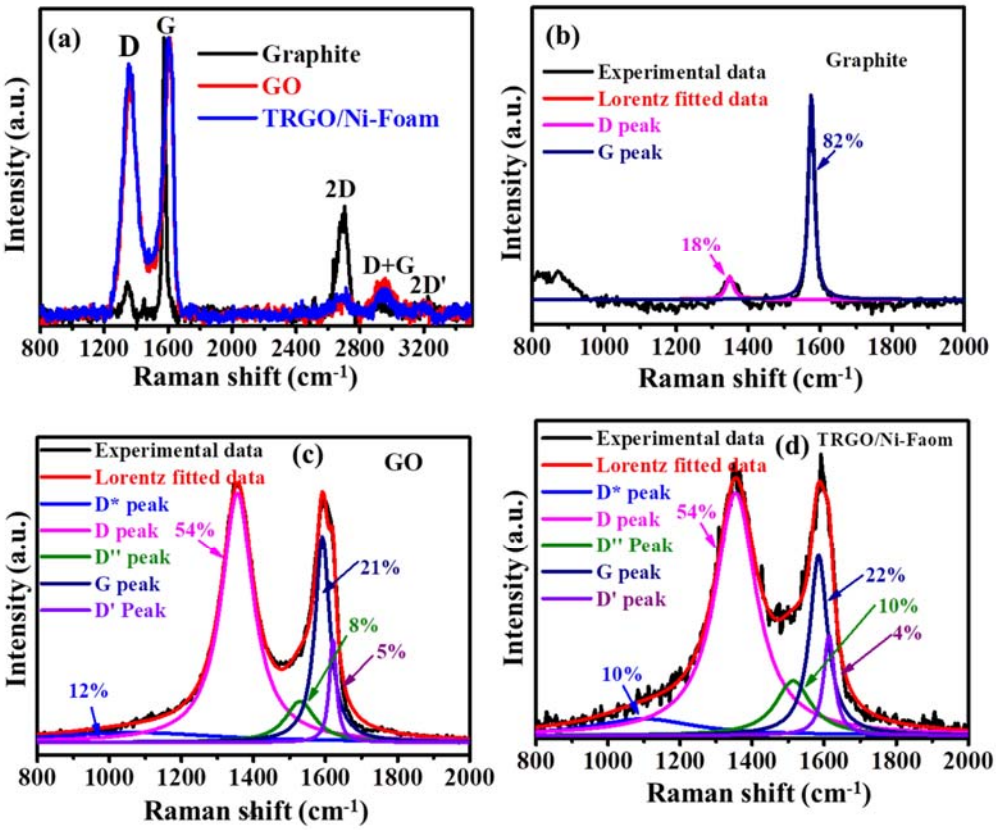

Fig. 4. (a) Raman spectra of graphite, GO and TRGO/NF and the deconvolution of (b) graphite, (c) GO and (d) TRGO/NF at the 800-2000 cm^{-1} region.

The images of the Raman mapping of integrated area (I_D/I_G) of the TRGO/NF is displayed in Fig. 5 (a). The image (Fig. 5(a)) shows a minimum and maximum value of 2.47 and 3.20 (average I_D/I_G is 2.77) indicating that the prepared TRGO/NF is indeed highly defective. Unlike, the images of graphene/NF displayed on Ref [72] which show a subtle I_D/I_G within the range of 0.0 – 0.5. The corresponding crystallite size (L_a) image estimated from the knight formula (1) is displayed in Fig. 5 (b). Emphasizing that indeed I_D/I_G is inversely proportional to the L_a as suggest by the Tuinstra – koenig model [70]. The intensity ratio of the defect – induced (I_D) peak relative to the defect-activated mode ($I_{D'}$) ($I_D/I_{D'}$) image is displayed in Fig. 5 (c). The red area is due to the sp^3 defects while the green area is due to the hopping defect like vacancy defects [62,73,74]. The image of the I_D/I_G+I_D (%) (Cuesta model [67]) in Fig. 5 (d) shows that the TRGO/NF is composed of highly defected reduced GO with a minimum and maximum of 71.21 and 76.2 (%). The I_D/I_G+I_D (%) and I_D/I_G in Fig 5 (a) show the same trend of defects.

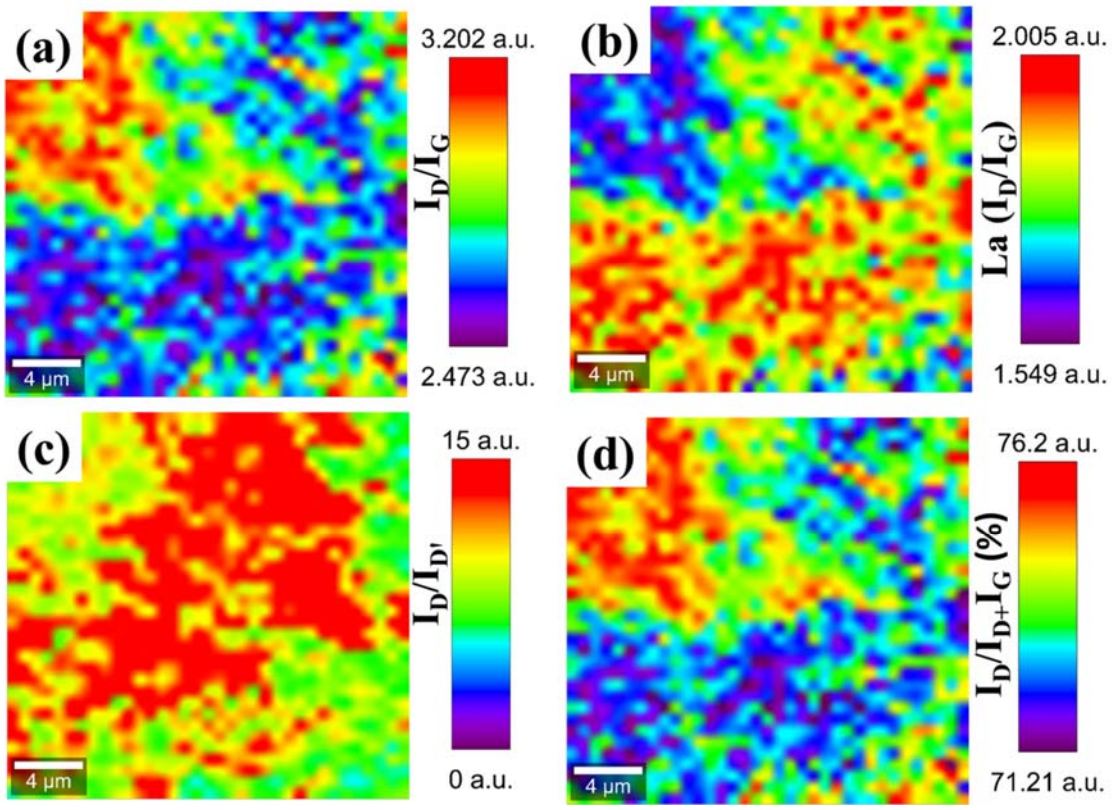

Fig. 5. Raman mapping of (a) I_D / I_G, crystallite size (L_a), (c) I_D / $I_{D'}$ and (d) I_D / I_D + I_G together with their colour scale.

The scanning electron microscopy image of graphite, GO, NF and TRGO/NF are displayed in Fig. 6. Graphite morphology in Fig. 6 (a) shows micro-particles similar to that of a pine tree (*Pinus pinaster*) bark with various dimensions. The high magnification inset to Fig. 6 (a) shows that the micro-particles are made of horizontally stacked planes. Fig. 6 (b) shows morphology of the dried GO showing the presence of randomly disordered stacked graphene sheets. The morphology of NF in Fig. 6 (c) showed a smooth surface and complex interconnected Ni-fibres. Morphology of TRGO\NF is displayed in Fig. 6 (d) which shows that the TRGO have adhered to the surface of NF. The TRGO is wrinkled as can be seen on Fig. 3 (a), resulted in a higher surface area contributing in a higher electrochemical performance.

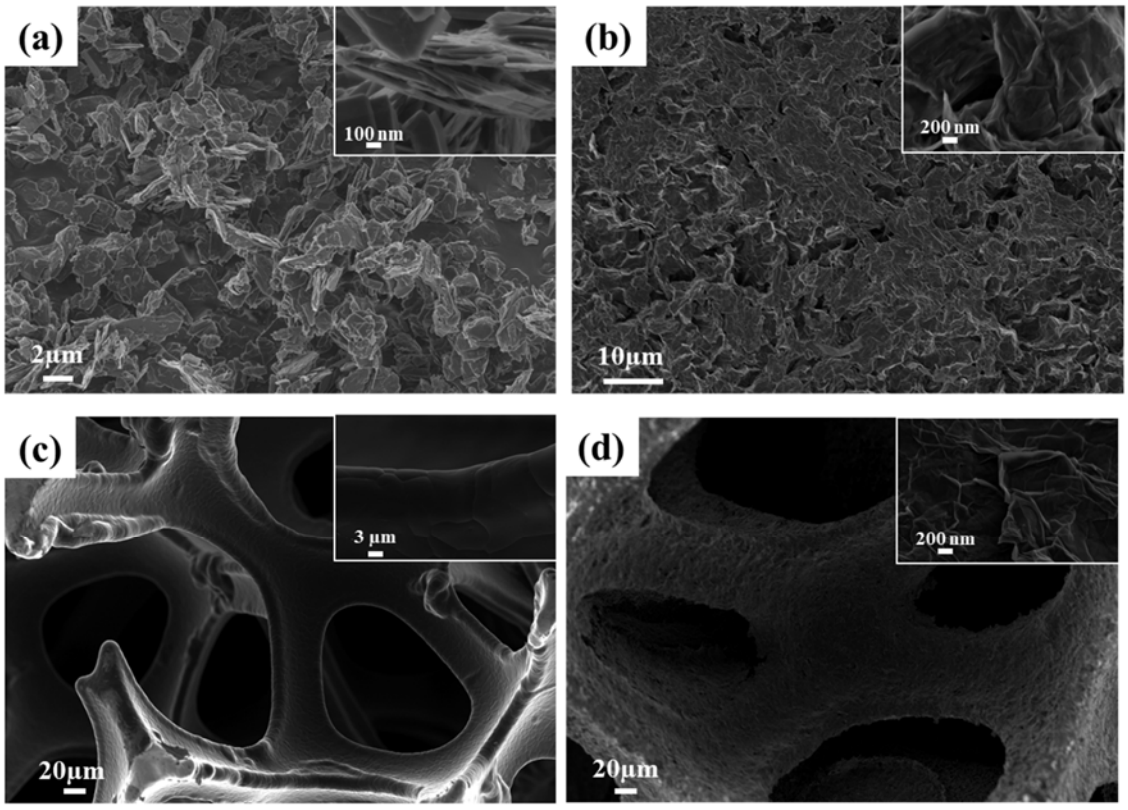

Fig. 6. SEM micrographs of (a) graphite, (b) GO, (c) NF and (d) TRGO/NF

3.2.Electrochemistry characterization

3.2.1. Three electrode configuration

The electrochemical performance of the TRGO/NF was evaluated in the three – electrode configuration in the positive potential window using three different electrolytes at a scan rate of 20 mV s^{-1} as shown in Fig. S2 (a). The 6 M KOH electrolyte showed a better performance (higher current response) compared to 1 M Na_2SO_4 and 1 M NaOH electrolytes due to the higher concentration and ionic conductivity of OH^- anions within the 6 M KOH electrolyte [55,75]. The GCD curve in Fig. S2 (b) also shows that the 6 M KOH shows the best electrochemical performance amongst other electrolytes. Fig. S2 (c) compares the CV at 20 mVs^{-1} of TRGO/NF to that of pure NF, the TRGO/NF has a higher current response than pure NF due to the TRGO embedded on the NF. The 6 M KOH electrolyte was used for

electrochemical evaluation throughout this study because it has shown much better electrochemical results as compared to other electrolytes for this electrode material. The electrochemical result that shows that the TRGO/NF reduced at 200 ℃ has a better performance than those reduced at higher temperature (400 and 800℃) are displayed in Fig. S3. This is due to the presence of residual functional groups such as carbonyl and quinone which provide passage for ions into the internal surface, pseudocapacitive behaviour enhancing the charge storage capability [16,27–29] and high wettability between the electrolyte and active material yielding better electrochemical performance [14,76]. These results are in line with those reported by Zhao et al. [16] where the GO reduced at 200 ℃ has the highest specific capacitance of 260.5 F g^{-1} at a discharge specific current of 0.4 A g^{-1} and the lowest capacitance was attainted from GO reduced at the highest temperature of 900 ℃. The capacitance of the TRGO micro-supercapacitor also decreased with increase in reducing temperature and the FTIR with that study indicated the removal of oxygen content [30]. The CV curves displayed in Fig. 7 (a) are showing some Faradic behaviour due to the interaction between the high concentration 6 M KOH electrolyte and the functional groups on the TRGO/NF [16,27]. This Faradic behaviour can also be seen on the GCD curve displayed in Fig. 7 (b). The specific capacity (Q_s) of the TRGO/NF was calculated from the GCD curve in Fig. 7 (b) using equation 2 below [32,72]

$$Q_s = \left(\frac{I}{m}\right)\frac{t}{3.6}\ [\text{mA h g}^{-1}] \qquad \ldots (2)$$

where I, m and t are current (mA), mass (mg) and discharge time (s), respectively. The specific capacity as a function of specific current is displayed in Fig. 7 (c) showing a specific capacity of 52.64 mA h g^{-1} at 0.5 A g^{-1} and a small reduction at 5 A g^{-1} which can be allotted to the limited time that ions have to access the surface of the electrode [16,72]. Ramadoss et al. [28] attributed the decrease of the capacitance as a function of specific current of the TRGO – coated fabric to the interruption of the charge diffusions of graphene for the time constraint for fast charge/discharge. This led to the activation of the outer surface resulting in decreased capacitance at high scan rate.

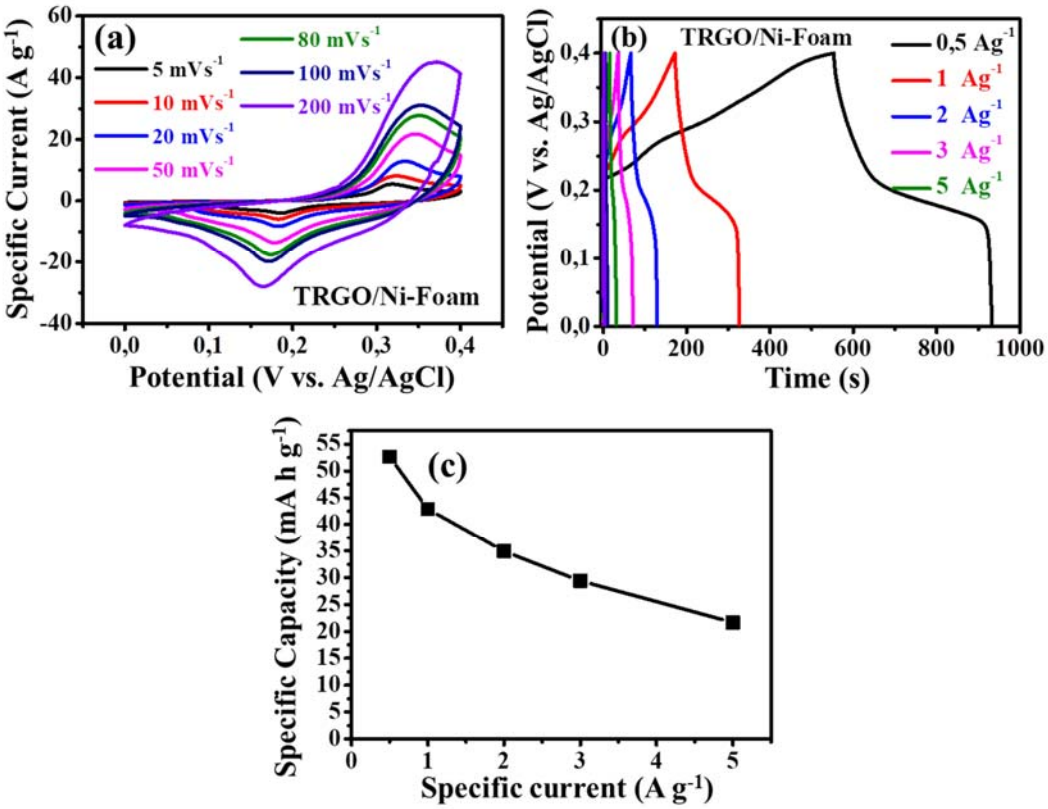

Fig. 7. (a) CV curves at various scan rates; (b) GCD curves at different specific currents and (c) specific capacity as a function of specific current for TRGO/NF sample

Based on the above discussed results, we have illustrated the preparation and advantage of the TRGO as a positive electrode in Fig. 8. Fig. 8 (a) – (c) shows the schematic of the transformation from graphite to TRGO. The schematic in Fig. 8 (a) shows of particles of graphite composed of sheets of graphene (see Fig. 6 (a) and its inset) and the small interspace distance determined from XRD on Fig. 2 (a), while the schematic of GO is presented on Fig. 8 (b). It is apparent that the spacing from the sheets has increased due to the attachment of the oxygen functional and intercalation of water (see Fig. 2). The XRD showed the increase of the interspace distance while the FTIR show the presence of oxygen functional groups, confirmed by the EDS showing the type of element constituting of those oxygen functional groups. Fig. 8 (c) shows the schematic of TRGO elucidating the decrease of oxygen functional groups together with the extermination of intercalated water and a slight decrease of the interplanar spacing. Fig. 8 (d) shows the schematic of graphite as a positive electrode and it is clear that the anion adhered on the surface of the graphite sheet. This behaviour is

responsible for the decrease of the electrochemical at high reducing temperature, since the oxygen content has been exterminated [16,30]. While on TRGO (Fig. 8 (e)) electrolyte anions have travelled into the bulk surface with the aid of the graphene oxygen surface functionality increasing the capacitance due to pseudocapacitive activity. Thus, the oxygen functional groups increase the wettability and also prevent the π - π interaction from restacking of graphene sheets. Our previous work [30] and that of Zhao et al. [16] also indicate the importance of the oxygen functional groups. Thus, oxygen content associated with reducing temperature of 200 ℃ leads to high energy and slightly low power. Moreover, unreduced GO and reduced GO with temperature below 200 ℃ leads to low energy and low power because of low electrical conductivity caused by high oxygen. GO reduced at above 200 ℃, have increasing high power (depending on the reducing temperature) and low energy due to dominance of EDLC behaviour. Thus, Low temperature TRGO has a better electrochemical due to the adequate residual oxygen functional groups.

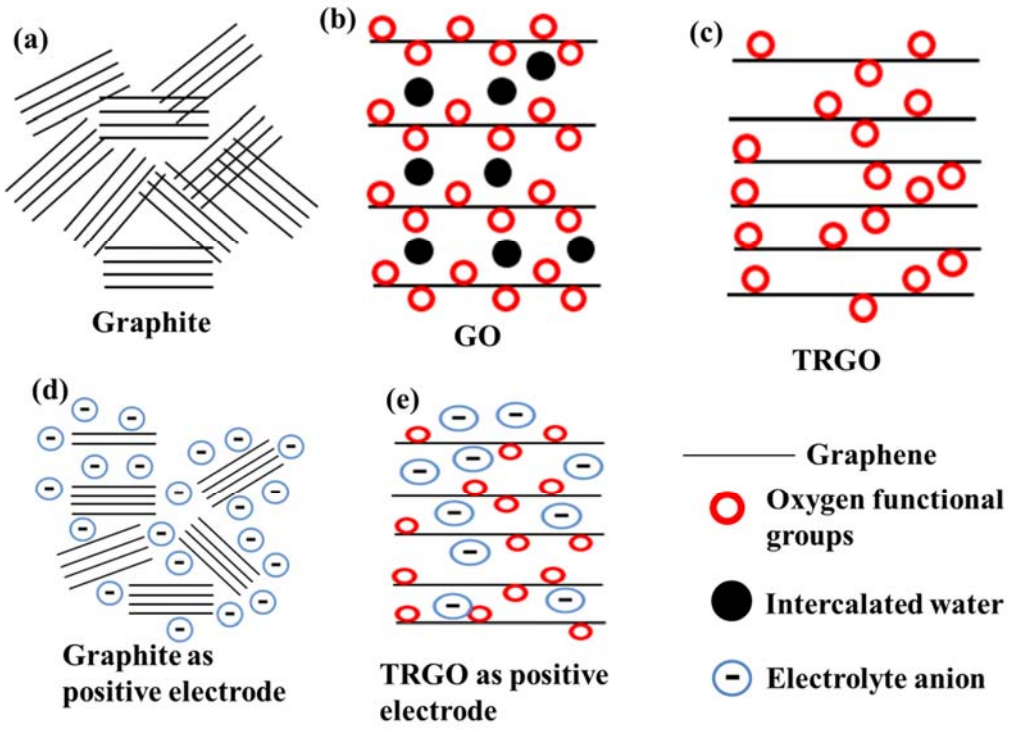

Fig. 8 schematic illustrating the (a) – (b) transformation from graphite to TRGO and interaction of electrolyte with (d) graphite and (e) TRGO as positive electrodes.

3.2.2. Two electrode configuration

Fig. 9 (a) shows an asymmetric supercapacitor device in a form of a coin cell with the TRGO/NF as a positive electrode and peanut shell activated carbon (PAC) as a negative material. The PAC electrode material was effectively analysed and reported by Sylla et al. [14]. The three electrode CV curve measurement of TRGO/NF and PAC in 6 M KOH electrolyte at 20 mV s^{-1} is displayed in Fig. 9 (b). TRGO/NF and PAC have positive and negative potential windows of 0 to 0.4 V and 0 to -0.9 V vs. Ag/AgCl, respectively. The charge balance was done using equations (S1) - (S3). The CV curves of the asymmetric device in Fig. 9 (c) were able to reach a maximum potential of 1.4 V which is greater than the combined potential windows of TRGO/NF and PAC in three electrode configurations. The CV curves of the device are asymmetric in shape, slightly distorted rectangular-like shape indicating electric double layer capacitor (EDLC) behaviour which is constant throughout the various scan rates, suggesting a good charge propagation and fast ionic transport [49]. The GCD curve obtained at various specific current displayed in Fig. 9 (d) also shows an EDLC behaviour throughout the different specific currents agreeing with the CV curves in Fig. 9 (c) confirming the good capacitive behaviour of the device. The absences of ohmic drops on the GCD curves indicate a low internal resistance [35,77]. The specific capacitance (C_s) was calculated using equation (3) below [14] due to its EDLC behaviour.

$$C_s = \frac{I_s \Delta t}{\Delta V} \text{ [F g}^{-1}\text{]} \quad \ldots (3)$$

where I_s , Δt and ΔV are the specific current (A g^{-1}), discharge time (s) and cell potential (V), respectively. The device specific capacitance was calculated to be 78.78 F g^{-1} at 1 A g^{-1} and displayed in Fig. 9 (e) showing rate capability of 80 % at 5 A g^{-1}. The specific capacitance drop at higher specific current is attributed to the limited time that ions have to access the surface of the electrode at a higher specific current [28,72]. The Ragone plot showing specific energy (E_s) as a function of specific power (P_s) is displayed in Fig. 9 (f) calculated from the GCD curve displayed in Fig. 9 (d) using equation (4) and (5), respectively.

$$E_s = \frac{I_s}{3.6} \int_{V_i}^{V_f} V \, dt \text{ [W h Kg}^{-1}\text{]} \quad \ldots (4)$$

$$P_s = \frac{E_s}{\Delta t} \times 3600 \text{ [W kg}^{-1}\text{]} \quad \ldots (5)$$

where I_s, $\int_{V_i}^{V_f} V \, dt$ and Δt are the specific current (A g^{-1}), integral under the area of the discharge time (V s) and discharge time (s), respectively. The device has a specific energy of

18.73 W h kg^{-1} at corresponding specific power of 547.52 W kg^{-1} at 1 A g^{-1} and a higher specific power of 2.5 kW kg^{-1} at a corresponding specific energy of 14.10 W h kg^{-1} at 5 A g^{-1}. These indicate stable device producing higher energy at a wide specific current. The obtained specific energy and power are higher and comparable to those previously reported TRGO and TRGO composites on conductive fabric and other metallic current collectors [28,29,35,49,77] (see Fig. 9 (f)). The previously reported studies displayed on the Ragone plot are also displayed in table 1. The table compares the steps, sample preparation, cell potential (Cp), capacitance retention (CR), electrolyte, specific energy (E_s) and specific power (E_s). The preparation of TRGO/NF requires one step from GO to electrochemical measureable electrode, whiles other requires 2 or more steps. This emphasis the simplicity of the preparation method, which is very safe since it does not requires any health threatening chemical such as hydrazine ($NH_2NH_2{\bullet}H_2O$). The table further shows that this method is not only simple but also produced a high performance supercapaitor device. The device showed a columbic efficiency (C_E) determined from equation (S4) (Fig. 9 (g)) of 99.9% indicating good reversibility and a capacitance retention (Fig. 9 (h)) of 70% after 16 000 cycles.

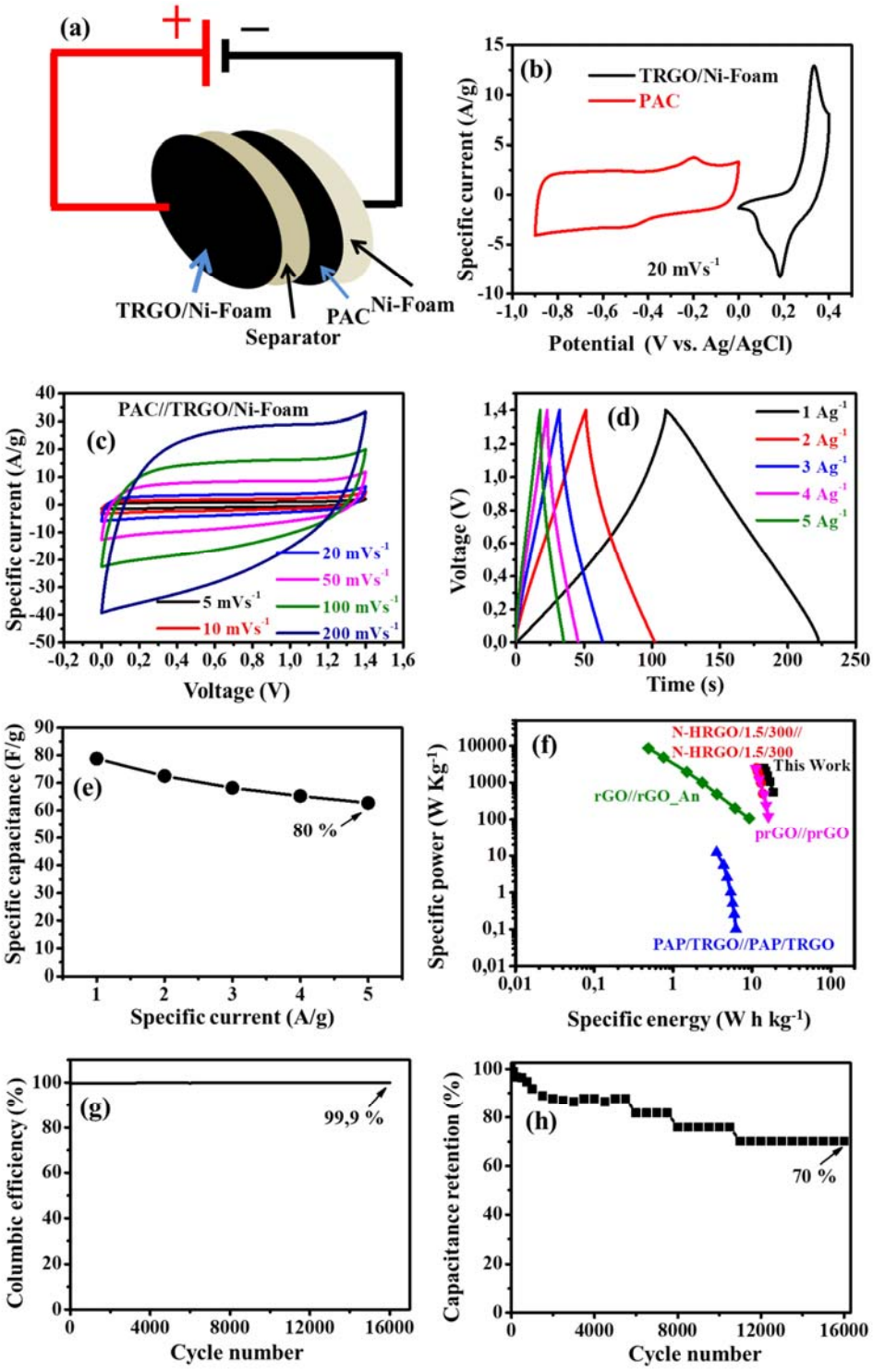

Fig. 9. TRGO/NF//PAC asymmetric (a) device schematic, (b) CV of positive and negative electrodes, (c) CV curves at different scan rates, (d) GCD curves at different specific currents, (e) specific capacitance versus specific current, (f) Ragone plot, (g) columbic efficiency and (h) capacitance retention

Device configuration	steps	Preparation conditions	Cp (V)	Electrolyte	CR @ C_d@ Cn (% @ A g^{-1} @ cycles)	E_s @ P_s @ C_d (W h kg^{-1} @ W kg^{-1} @ A g^{-1})	Ref.
TRGO/Ni-Foam//PAC	1	GO was slurry pasted on Ni-Foam then thermally reduced at 200℃ for an hour at heating rate of 10 ℃ min^{-1} under Ar	1.4	6 M KOH	70 @ 5@ 16 000	18.73 @ 547.52 @ 1 Ag^{-1}	This work
PAP/TRGO20†	3	Graphite oxide was thermal treated at 700 ℃ under N_2 flow at heating rate of 5 ℃ min^{-1}. Then used with pyrrole and aniline to create PAP/TRGO	1.0	1 M H_2SO_4	103 @ 1 @ 10 000	6.3 @ 100 @ 0.2	[49]
TRGO-coated FSSS†	1	GO was repeated dip-coated onto a conductive fabric and dried at 60 ℃ for 30 min. Then thermal treated at 160 ℃ in Ar for 2 h	1.0	PVA/ H_3PO_4	93 @ 2.5 mA cm^{-2} @1 000 S	5.8 @ 27.7 k @ 0.1 mA cm^{-2}	[28]
N-HRGO/1.5/300†	3	HGO was chemical etched from GO using H_2O_2 and heating at 100 ℃ for 1.5 h, then centrifuge and washed. HGO was mixed with PPD and stirred for 2 h, and then vacuum filtrated. Membrane was freeze-dried for 12 h and lastly annealed at 300 ℃ at 5 ℃ min-1 under Ar.	1.0	6 M KOH	89.3 @ 2 @ 5 000	14.0 @ 500 @ 0.5	[35]
rGO//rGO_An	2	rGO was obtained from mixing aqueous GO with NH_3 and NH_2NH_2•H_2O, the heat at 95℃ under string for 45 min. Then thermal annealed at 280 ℃ under Ar atmosphere for 1 h	1.0	PVA – 2 M KOH	91.1 @ 2 @ 1 000	9.26 @ 8.8 k @0.5	[77]
prGO†	3	ZnO powder was dispersed into GO aqueous solution, stirred overnight and sonicated for 1 h in ice bath. Then filtered and dried at 40 ℃. The obtained GO/ZnO powders was dispersed in EG and HCl and microwave irradiated for 6 min at 180 ℃ then filtered and washed to obtain prGO.	1.0	1 M H_2SO_4	–	15.0 @ 250 @ 1	[29]

Abbreviations: Cp – cell potential, C_s – specific current, Cn – cycle number, CR – capacitance retention, PAC – peanut shell activated carbon, PAP – poly(aniline-co-pyrrole, FSSS – fabric solid state supercapacitor, N-HRGO/1.5/300 – N-rich holey reduced graphene oxide, prGO – porous reduced graphene oxide, † – symmetric device, s – single electrode and k – kilo

Table 1. Supercapacitor preparation conditions and electrochemical performance comparison between various thermally reduced GO materials reported in the literature and TRGO/NF in this work.

The electrical properties of the TRGO/NF//PAC device was analysed using EIS, as shown by Nyquist plot displayed in Fig. 10 (a). The EIS also determines the nature of the active material on the electrode/electrolyte interface. This Nyquist plot lacks a higher region frequency semi – circle suggesting a low electrode/electrolyte interface charge transfer resistance suggesting a better capacitive behaviour [15]. The reported Nyquist is similar to the ideal supercapacitive behaviour, with a short 45° line starting from the equivalent series resistance (ESR) transitioning into the fast increase close to being parallel to the imaginary impedance (-Im Z) axis [15,78]. The Nyquist plot line being near parallel to the imaginary impedance (-Im Z) axis, is indication of the device being highly capacitive. The real impedance (Re Z) axis intercept in the high frequency region indicates the ESR of 1.6 Ω describing the interfacial contact resistance between the active materials and NF current collector, electrode/electrolyte interface and the internal resistance of the active material [14,15]. The low ESR agrees with the absence of ohmic drop in Fig 9 (d). Thus, The EIS confirms the device CV and GCD. The maximum power, P_{max} of the device was estimated from equation (6) below to be 306.25 kW kg^{-1}

$$P_{max} = \frac{\Delta V^2}{4m(ESR)} \text{ [W kg}^{-1}\text{]} \quad \ldots (6)$$

where ΔV, m and ESR are the cell potential (V), mass (of 4×10^{-6} kg) and ESR of 1.6 Ω determined from the Nyquist plot in Fig. 10 (a), respectively. The Nyquist plot was fitted using the equivalent circuit diagram shown in Fig. 10 (b) and the chi-square (χ^2) was 2.404 indicating a very good fitness. The equivalent circuit diagram shows the presence of the ESR connected in series to capacitor (C) and Warburg impedance (W). A deviation of the Nyquist plot from the imaginary axis is attributed to the leakage resistance R_L which is quite minimum in this case because the deviation from y – axis is not that much. The good capacitive behaviour seen on the CV (Fig. 9 (c)), GCD (Fig. 9 (d)) curves and Nyquist plot (Fig .10 (a)) is confirmed by the phase angle of – 86° displayed in Fig. 10 (c) of which is very close to the ideal phase angel of – 90 ° [79]. The frequency dependent real ($C'(\omega)$) and imaginary ($C''(\omega)$) capacitances are displayed in Fig. 10 (d) calculated from equation (7) – (10) where the impedance $Z(\omega)$ with $\omega = 2\pi f$ is expressed as

$$Z(\omega) = \frac{1}{j\omega \times C(\omega)} \quad \ldots (7)$$

$$C'(\omega) = \frac{Z''(\omega)}{\omega |Z(\omega)|^2} \quad \ldots (8)$$

$$C''(\omega) = \frac{Z\prime(\omega)}{\omega|Z(\omega)|^2} \quad \ldots (9)$$

$$|Z(\omega)|^2 = Z'(\omega)^2 + Z''(\omega)^2 \quad \ldots (10)$$

Fig. 10 (d) also shows that the real ($C'(\omega)$) accessible capacitance of 1.0 F and the imaginary $C''(\omega)$ gives a relaxation time ($\tau = 1/2\pi f$, where f is the peak of the frequency) of 0.39 s suggesting that the prepared device can be quickly charged. All of the aforementioned results confirm the outstanding electrochemical performance of TRGO/Ni-Foam as a suitable positive electrode for SC due to the following factors: (1) nano – graphene sheets are directly deposited on Ni Foam forming an integrated binder – free electrode improving the electrical conductivity between TRGO active material and Ni-Foam current collector, reducing resistance and facilitating a fast electrochemical reaction rate; (2) TRGO loosely stacked provides a large accessible surface area and allows access of ions during adsorption/desorption leading to more efficient transport; (3) surface oxygen functional groups serve as a passage to the bulker material and provide some pseudocapacitance and increase the charge caring capabilities and (4) the high conducting TRGO provided an effective pathway for charge transport. These suggest that TRGO/Ni-Foam hold great promise for supercapacitor devices.

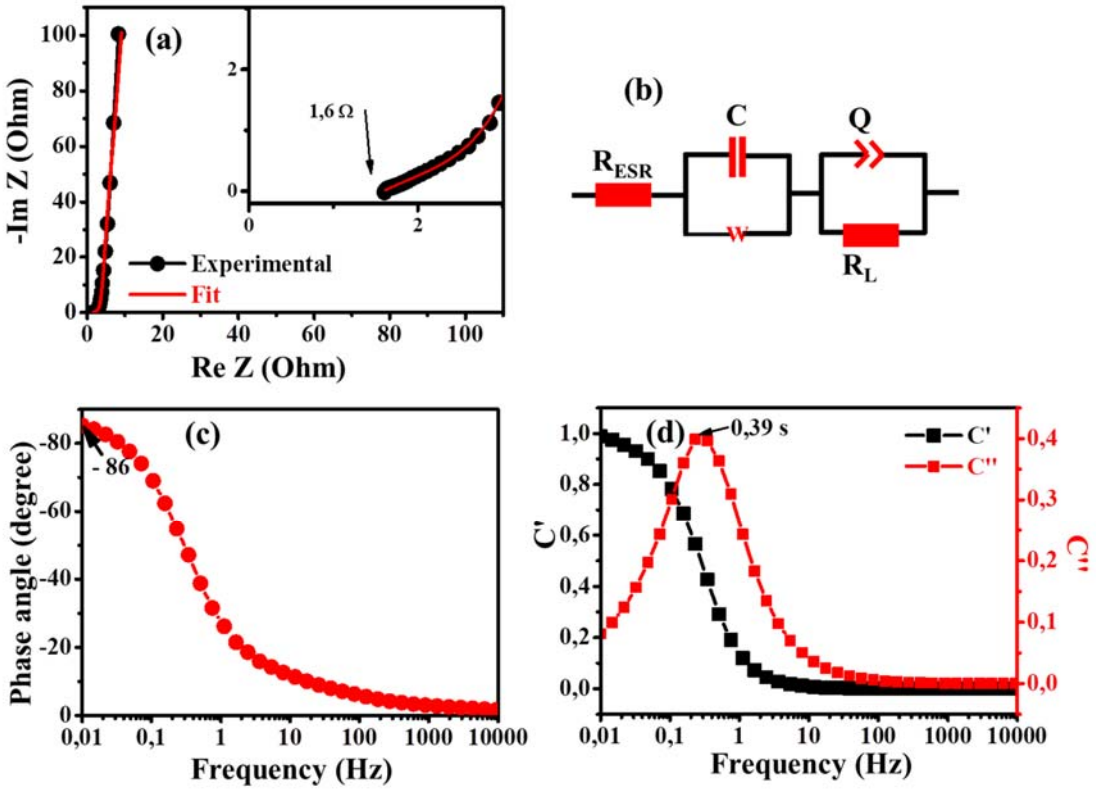

Fig. 10. (a) Nyquist plot of the device (the inset shows the enlarged high-frequency region of the plot), (b) equivalent circuit diagram used to fit the Nyquist plot in (c) (i.e. a red solid-line), (c) phase angle versus frequency and (d) real and imaginary plot of capacitance as a function of frequency.

4. Conclusion

In summary, additive (binder and conducive enhances) free TRGO/NF electrode was successfully prepared using a low temperature one step AP-CVD at 200 ℃ for an hour. The SEM showed the adhesion of graphene sheets on the surface of NF. Raman images show the dispersion of graphitization, also emphasized that Tuinsta – Koenig and Cuesta models show a similar defect distribution. Absence of conductive enhance and binder allowed the determination of the real electrochemical performance. The presence of oxygen content significantly increased electrochemical performance of the positive TRGO electrode. The two electrode (device) showed a high specific capacitance of 78.78 F g^{-1} at 1 A g^{-1} with the corresponding specific energy and power of 18.73 W h kg^{-1} and 547.52 W kg^{-1}, respectively. The specific energy and power at 5 A g^{-1} was estimated to be 14.10 W h kg^{-1} and 2.5 kW kg^{-1}, respectively. The maximum power from the device was estimated to be 306.25 kW kg^{-1}.

The EIS showed that the device is highly capacitive due to lack of a semi-circle and high phase angle of – 86 °

Acknowledgements

This work was supported by the National Research Foundation (NRF) of South Africa through the South African Research Chairs Initiative (SARChI) (Grant Number 61056). Any idea, finding, conclusion or recommendation expressed in this publication is that of the author(s). The NRF does not accept any liability in this regard. V.M. Maphiri acknowledges NRF bursary through SARChI in Carbon Technology and Materials and University of Pretoria for his studies.

References

[1] Z. Peng, Q. Jiang, P. Peng, F. Li, Nh3-activated fullerene derivative hierarchical microstructures to porous fe3o4/n-c for oxygen reduction reaction and zn-air battery, Eng. Sci. 14 (2021) 27–38. https://doi.org/10.30919/ES8D1311.

[2] Z. Mohamed, G. Zhang, B. He, Y. Fan, Heterostructure Necklace-like NiO-NiCo2O4 Hybrid with Superior Catalytic Capability as Electrocatalyst for Li-Oxygen Batteries, Eng. Sci. 17 (2022) 231–241. https://doi.org/10.30919/ES8D595.

[3] C. Lai, Y. Wang, L. Fu, H. Song, B. Liu, D. Pan, Z. Guo, I. Seok, K. Li, H. Zhang, M. Dong, Aqueous flexible all-solid-state NiCo-Zn batteries with high capacity based on advanced ion-buffering reservoirs of NiCo 2 O 4, (n.d.). https://doi.org/10.1007/s42114-021-00375-1.

[4] Y. Zhang, Y. An, L. Wu, H. Chen, Z. Li, H. Dou, V. Murugadoss, J. Fan, X. Zhang, X. Mai, Z. Guo, Metal-free energy storage systems: combining batteries with capacitors based on a methylene blue functionalized graphene cathode, J. Mater. Chem. A. 7 (2019) 19668–19675. https://doi.org/10.1039/C9TA06734E.

[5] J. Zhao, D. Wei, C. Zhang, Q. Shao, V. Murugadoss, Z. Guo, Q. Jiang, X. Yang, An overview of oxygen reduction electrocatalysts for rechargeable zinc-air batteries

enabled by carbon and carbon composites, Eng. Sci. 15 (2021) 1–19. https://doi.org/10.30919/ES8D420.

[6] M.T. Dizaji, W. Li, Higher voltage redox flow batteries with hybrid acid and base electrolytes, Eng. Sci. 11 (2020) 54–65. https://doi.org/10.30919/ES8D1118.

[7] C. Hou, B. Wang, V. Murugadoss, S. Vupputuri, Y. Chao, Z. Guo, C. Wang, W. Du, Recent advances in Co3O4as anode materials for high-performance lithium-ion batteries, Eng. Sci. 11 (2020) 19–30. https://doi.org/10.30919/ES8D1128.

[8] L. Liu, C. Wang, Z. He, R. Das, B. Dong, X. Xie, Z. Guo, An overview of amphoteric ion exchange membranes for vanadium redox flow batteries, J. Mater. Sci. Technol. 69 (2021) 212–227. https://doi.org/10.1016/J.JMST.2020.08.032.

[9] X. Jiang, Y. Chen, X. Meng, W. Cao, C. Liu, Q. Huang, N. Naik, V. Murugadoss, M. Huang, Z. Guo, The impact of electrode with carbon materials on safety performance of lithium-ion batteries: A review, Carbon N. Y. 191 (2022) 448–470. https://doi.org/10.1016/J.CARBON.2022.02.011.

[10] Z. Liu, G. Li, Q. Qin, L. Mi, G. Li, G. Zheng, C. Liu, Q. Li, X. Liu, Electrospun PVDF/PAN membrane for pressure sensor and sodium-ion battery separator, Adv. Compos. Hybrid Mater. 4 (2021) 1215–1225. https://doi.org/10.1007/S42114-021-00364-4/FIGURES/6.

[11] X. Dong, X. Zhao, Y. Chen, C. Wang, Investigations about the influence of different carbon matrixes on the electrochemical performance of Na3V2(PO4)3 cathode material for sodium ion batteries, Adv. Compos. Hybrid Mater. 4 (2021) 1070–1081. https://doi.org/10.1007/S42114-021-00319-9/FIGURES/10.

[12] G. Li, C. Dang, Y. Hou, F. Dang, Y. Fan, Z. Guo, Experimental and theoretical characteristic of single atom Co-N-C catalyst for Li-O2 batteries, Eng. Sci. 10 (2020) 85–94. https://doi.org/10.30919/ES8D1005.

[13] D.J. Tarimo, K.O. Oyedotun, A.A. Mirghni, N.F. Sylla, N. Manyala, High energy and excellent stability asymmetric supercapacitor derived from sulphur-reduced graphene oxide/manganese dioxide composite and activated carbon from peanut shell, Electrochim. Acta. 353 (2020) 136498. https://doi.org/10.1016/j.electacta.2020.136498.

[14] N.F. Sylla, N.M. Ndiaye, B.D. Ngom, D. Momodu, M.J. Madito, B.K. Mutuma, N. Manyala, Effect of porosity enhancing agents on the electrochemical performance of high-energy ultracapacitor electrodes derived from peanut shell waste, Sci. Rep. 9 (2019) 1–15. https://doi.org/10.1038/s41598-019-50189-x.

[15] T.S. Mathis, N. Kurra, X. Wang, D. Pinto, P. Simon, Y. Gogotsi, Energy Storage Data Reporting in Perspective—Guidelines for Interpreting the Performance of Electrochemical Energy Storage Systems, Adv. Energy Mater. 9 (2019) 1–13. https://doi.org/10.1002/aenm.201902007.

[16] B. Zhao, P. Liu, Y. Jiang, D. Pan, H. Tao, J. Song, T. Fang, W. Xu, Supercapacitor performances of thermally reduced graphene oxide, J. Power Sources. 198 (2012) 423–427. https://doi.org/10.1016/j.jpowsour.2011.09.074.

[17] S.S. Patil, T.S. Bhat, A.M. Teli, S.A. Beknalkar, S.B. Dhavale, M.M. Faras, M.M. Karanjkar, P.S. Patil, Hybrid Solid State Supercapacitors (HSSC's) for High Energy & Power Density: An Overview, Eng. Sci. 12 (2020) 38–51. https://doi.org/10.30919/ES8D1140.

[18] S. ur Rehman, R. Ahmed, K. Ma, S. Xu, T. Tao, M.A. Aslam, M. Amir, J. Wang, Composite of strip-shaped ZIF-67 with polypyrrole: A conductive polymer-MOF electrode system for stable and high specific capacitance, Eng. Sci. 13 (2021) 71–78. https://doi.org/10.30919/ES8D1263.

[19] X. Jiang, Z. Li, J. Yao, Z. Shao, X. Chen, One-step synthesis of soy protein/graphene nanocomposites and their application in photothermal therapy, Mater. Sci. Eng. C. 68 (2016) 798–804. https://doi.org/10.1016/j.msec.2016.07.034.

[20] L. Qiu, H. Zhang, W. Wang, Y. Chen, R. Wang, Effects of hydrazine hydrate treatment on the performance of reducedgraphene oxide film as counter electrode in dye-sensitized solar cells, Appl. Surf. Sci. 319 (2014) 339–343. https://doi.org/10.1016/j.apsusc.2014.07.133.

[21] P. Zhu, M. Shen, S. Xiao, D. Zhang, Experimental study on the reducibility of graphene oxide by hydrazine hydrate, Phys. B Condens. Matter. 406 (2011) 498–502. https://doi.org/10.1016/j.physb.2010.11.022.

[22] S. Park, H. Lee, Y.-J. Kim, P.S. Lee, Fully laser-patterned stretchable

microsupercapacitors integrated with soft electronic circuit components, NPG Asia Mater. 10 (2018) 959–969. https://doi.org/10.1038/s41427-018-0080-z.

[23] M. Gao, X. Dong, K. Wang, W. Duan, X. Sun, C. Zhu, W. Wang, Laser direct preparation and processing of graphene/MnO nanocomposite electrodes for microsupercapacitors, J. Energy Storage. 33 (2021) 102162. https://doi.org/10.1016/j.est.2020.102162.

[24] O. Mondal, S. Mitra, M. Pal, A. Datta, S. Dhara, D. Chakravorty, Reduced graphene oxide synthesis by high energy ball milling, Mater. Chem. Phys. 161 (2015) 123–129. https://doi.org/10.1016/j.matchemphys.2015.05.023.

[25] P. Vázquez-Sánchez, M.A. Rodríguez-Escudero, F.J. Burgos, I. Llorente, O. Caballero-Calero, M.M. González, R. Fernández, M.C. García-Alonso, Synthesis of Cu/rGO composites by chemical and thermal reduction of graphene oxide, J. Alloys Compd. 800 (2019) 379–391. https://doi.org/10.1016/j.jallcom.2019.06.008.

[26] K.K.H. De Silva, H.H. Huang, R. Joshi, M. Yoshimura, Restoration of the graphitic structure by defect repair during the thermal reduction of graphene oxide, Carbon N. Y. 166 (2020) 74–90. https://doi.org/10.1016/j.carbon.2020.05.015.

[27] Q. Du, M. Zheng, L. Zhang, Y. Wang, J. Chen, L. Xue, W. Dai, G. Ji, J. Cao, Preparation of functionalized graphene sheets by a low-temperature thermal exfoliation approach and their electrochemical supercapacitive behaviors, Electrochim. Acta. 55 (2010) 3897–3903. https://doi.org/10.1016/j.electacta.2010.01.089.

[28] A. Ramadoss, B. Saravanakumar, S.J. Kim, Thermally reduced graphene oxide-coated fabrics for flexible supercapacitors and self-powered systems, Nano Energy. 15 (2015) 587–597. https://doi.org/10.1016/J.NANOEN.2015.05.009.

[29] J. Ma, Y. Yamamoto, C. Su, S. Badhulika, C. Fukuhara, C.Y. Kong, One-pot microwave-assisted synthesis of porous reduced graphene oxide as an electrode material for high capacitance supercapacitor, Electrochim. Acta. 386 (2021) 138439. https://doi.org/10.1016/J.ELECTACTA.2021.138439.

[30] V.M. Maphiri, G. Rutavi, N.F. Sylla, S.A. Adewinbi, O. Fasakin, N. Man-, Novel Thermally Reduced Graphene Oxide Microsupercapacitor Fabricated via Mask — Free AxiDraw Direct Writing, (2021) 1–15.

[31] M.J. Madito, K.S. Matshoba, F.U. Ochai-Ejeh, N. Mongwaketsi, C.B. Mtshali, M. Fabiane, N. Manyala, Nickel-copper graphene foam prepared by atmospheric pressure chemical vapour deposition for supercapacitor applications, Surf. Coatings Technol. 383 (2020) 125230. https://doi.org/10.1016/j.surfcoat.2019.125230.

[32] D.J. Tarimo, K.O. Oyedotun, A.A. Mirghni, N. Manyala, Sulphur-reduced graphene oxide composite with improved electrochemical performance for supercapacitor applications, Int. J. Hydrogen Energy. 45 (2020) 13189–13201. https://doi.org/10.1016/j.ijhydene.2020.03.059.

[33] Z. Zhu, S. Tang, J. Yuan, X. Qin, Y. Deng, R. Qu, G.M. Haarberg, Effects of Various Binders on Supercapacitor Performances, Int. J. Electrochem. Sci. 11 (2016) 8270–8279. https://doi.org/10.20964/2016.10.04.

[34] B. Xu, H. Wang, Q. Zhu, N. Sun, B. Anasori, L. Hu, F. Wang, Y. Guan, Y. Gogotsi, Reduced graphene oxide as a multi-functional conductive binder for supercapacitor electrodes, Energy Storage Mater. 12 (2018) 128–136. https://doi.org/10.1016/j.ensm.2017.12.006.

[35] Y. Xu, C. Huang, A. Hu, Z. Fan, C. Chen, Y. Yang, Q. Tang, C. Jiang, X. Chen, N-rich reduced graphene oxide film with cross-coupled porous networks as free-standing electrode for high performance supercapacitors, Appl. Surf. Sci. 563 (2021) 150303. https://doi.org/10.1016/J.APSUSC.2021.150303.

[36] T. Giannakopoulou, N. Todorova, A. Erotokritaki, N. Plakantonaki, A. Tsetsekou, C. Trapalis, Electrochemically deposited graphene oxide thin film supercapacitors: Comparing liquid and solid electrolytes, Appl. Surf. Sci. 528 (2020) 146801. https://doi.org/10.1016/j.apsusc.2020.146801.

[37] P. Xie, Y. Liu, M. Feng, M. Niu, C. Liu, N. Wu, K. Sui, R.R. Patil, D. Pan, Z. Guo, R. Fan, Hierarchically porous Co/C nanocomposites for ultralight high-performance microwave absorption, Adv. Compos. Hybrid Mater. 4 (2021) 173–185. https://doi.org/10.1007/S42114-020-00202-Z/FIGURES/9.

[38] H. Wu, H. Sun, F. Han, P. Xie, Y. Zhong, B. Quan, Y. Zhao, C. Liu, R. Fan, Z. Guo, Negative Permittivity Behavior in Flexible Carbon Nanofibers-Polydimethylsiloxane Films, Eng. Sci. 17 (2022) 113–120. https://doi.org/10.30919/ES8D576.

[39] H. Wu, Y. Zhong, Y. Tang, Y. Huang, G. Liu, W. Sun, P. Xie, D. Pan, C. Liu, Z. Guo, Precise regulation of weakly negative permittivity in CaCu3Ti4O12 metacomposites by synergistic effects of carbon nanotubes and grapheme, Adv. Compos. Hybrid Mater. 5 (2022) 419–430. https://doi.org/10.1007/S42114-021-00378-Y/FIGURES/5.

[40] G. Qi, Y. Liu, L. Chen, P. Xie, D. Pan, Z. Shi, B. Quan, Y. Zhong, C. Liu, R. Fan, Z. Guo, Lightweight Fe3C@Fe/C nanocomposites derived from wasted cornstalks with high-efficiency microwave absorption and ultrathin thickness, Adv. Compos. Hybrid Mater. 4 (2021) 1226–1238. https://doi.org/10.1007/S42114-021-00368-0/FIGURES/8.

[41] Y. Wang, Y. Liu, C. Wang, H. Liu, J. Zhang, J. Lin, J. Fan, T. Ding, J.E. Ryu, Z. Guo, Significantly enhanced ultrathin NiCo-based MOF nanosheet electrodes hybrided with Ti3C2Tx MXene for high performance asymmetric supercapacitors, Eng. Sci. 9 (2020) 50–59. https://doi.org/10.30919/ES8D903.

[42] Z. Sun, H. Qi, M. Chen, S. Guo, Z. Huang, S. Maganti, V. Murugadoss, M. Huang, Z. Guo, Progress in Cellulose/Carbon Nanotube Composite Flexible Electrodes for Supercapacitors, Eng. Sci. (2021). https://doi.org/10.30919/ES8D588.

[43] S. Li, J. Fan, S. Li, H. Jin, W. Luo, Y. Ma, J. Wu, Z. Chao, N. Naik, D. Pan, Z. Guo, Synthesis of Three dimensional Mo-Doped Nickel Sulfide Mesoporous Nanostructures/Ni Foam Composite for Supercapacitor and Overall Water Splitting, ES Energy Environ. (2022). https://doi.org/10.30919/ESEE8C646.

[44] P.M. Mana, P.K. Bhujbal, H.M. Pathan, Fabrication and Characterization of ZnS based Photoelectrochemical Solar Cell, ES Energy Environ. (2020). https://doi.org/10.30919/ESEE8C1021.

[45] Y. Liu, Y. Wang, H. Wang, P. Zhao, H. Hou, L. Guo, Acetylene black enhancing the electrochemical performance of NiCo-MOF nanosheets for supercapacitor electrodes, Appl. Surf. Sci. 492 (2019) 455–463. https://doi.org/10.1016/j.apsusc.2019.06.238.

[46] J. Sun, Y. Zhang, Y. Liu, H. Jiang, X. Dong, T. Hu, C. Meng, Hydrated vanadium pentoxide/reduced graphene oxide-polyvinyl alcohol (V2O5·nH2O/rGO-PVA) film as a binder-free electrode for solid-state Zn-ion batteries, J. Colloid Interface Sci. 587 (2021) 845–854. https://doi.org/10.1016/j.jcis.2020.10.148.

[47] N. Sun, Y. Guan, Y.T. Liu, Q. Zhu, J. Shen, H. Liu, S. Zhou, B. Xu, Facile synthesis of free-standing, flexible hard carbon anode for high-performance sodium ion batteries using graphene as a multi-functional binder, Carbon N. Y. 137 (2018) 475–483. https://doi.org/10.1016/j.carbon.2018.05.056.

[48] N. Radha, A. Kanakaraj, H.M. Manohar, M.R. Nidhi, D. Mondal, S.K. Nataraj, D. Ghosh, Binder free self-standing high performance supercapacitive electrode based on graphene/titanium carbide composite aerogel, Appl. Surf. Sci. 481 (2019) 892–899. https://doi.org/10.1016/j.apsusc.2019.03.086.

[49] A. Moyseowicz, Z. González, R. Menéndez, G. Gryglewicz, Three-dimensional poly(aniline-co-pyrrole)/thermally reduced graphene oxide composite as a binder-free electrode for high-performance supercapacitors, Compos. Part B Eng. 145 (2018) 232–239. https://doi.org/10.1016/j.compositesb.2018.03.018.

[50] D. Dsilva Winfred Rufuss, S. Iniyan, L. Suganthi, P.A. Davies, Low mass fraction impregnation with graphene oxide (GO) enhances thermo-physical properties of paraffin for heat storage applications, Thermochim. Acta. 655 (2017) 226–233. https://doi.org/10.1016/J.TCA.2017.07.005.

[51] H. Yin, D. Wang, H. Zhu, W. Xiao, F. Gan, Growing highly capacitive nano-Ni(OH)2 on freshly cut graphite electrode by electrochemically enhanced self-assembly, Electrochim. Acta. 99 (2013) 198–203. https://doi.org/10.1016/J.ELECTACTA.2013.03.137.

[52] S. Claramunt, A. Varea, D. Lópezlópez-Díaz, M. Mercedes Velázquezvelázquez, A. Cornet, A. Cirera, The Importance of Interbands on the Interpretation of the Raman Spectrum of Graphene Oxide, J. Phys. Chem. C. 119 (2015) 10123–10129. https://doi.org/10.1021/acs.jpcc.5b01590.

[53] R. Siburian, H. Sihotang, S. Lumban Raja, M. Supeno, C. Simanjuntak, New route to synthesize of graphene nano sheets, Orient. J. Chem. 34 (2018) 182–187. https://doi.org/10.13005/ojc/340120.

[54] Y. Wei, Y. Wang, L. Wei, X. Zhao, X. Zhou, H. Liu, Highly efficient and reactivated electrocatalyst of ruthenium electrodeposited on nickel foam for hydrogen evolution from NaBH4 alkaline solution, Int. J. Hydrogen Energy. 43 (2018) 592–600. https://doi.org/10.1016/j.ijhydene.2017.11.010.

[55] M.N. Rantho, M.J. Madito, N. Manyala, Symmetric supercapacitor with supercapattery behavior based on carbonized iron cations adsorbed onto polyaniline, Electrochim. Acta. 262 (2018) 82–96. https://doi.org/10.1016/j.electacta.2018.01.001.

[56] G.K. Veerasubramani, K. Krishnamoorthy, S.J. Kim, Improved electrochemical performances of binder-free CoMoO4 nanoplate arrays@Ni foam electrode using redox additive electrolyte, J. Power Sources. 306 (2016) 378–386. https://doi.org/10.1016/j.jpowsour.2015.12.034.

[57] Y. Li, Z. Hai, X. Hou, H. Xu, Z. Zhang, D. Cui, C. Xue, B. Zhang, Self-Assembly of 3D Fennel-Like Co3O4 with Thirty-Six Surfaces for High Performance Supercapacitor, J. Nanomater. 2017 (2017). https://doi.org/10.1155/2017/1404328.

[58] M. Bera, Chandravati, P. Gupta, P.K. Maji, Facile One-Pot Synthesis of Graphene Oxide by Sonication Assisted Mechanochemical Approach and Its Surface Chemistry, J. Nanosci. Nanotechnol. 18 (2017) 902–912. https://doi.org/10.1166/jnn.2018.14306.

[59] M. Muniyalakshmi, K. Sethuraman, D. Silambarasan, Synthesis and characterization of graphene oxide nanosheets, Mater. Today Proc. 21 (2020) 408–410. https://doi.org/10.1016/j.matpr.2019.06.375.

[60] Z. Liu, Z. Diao, Y. Yuan, H. Jia, L. Wang, W. Fei, A two-step thermal treatment method to produce reduced graphene oxide with selectively increasing electrochemically active carbonyl group content for high-performance supercapacitor electrode, Colloids Surfaces A Physicochem. Eng. Asp. 620 (2021) 126573. https://doi.org/10.1016/j.colsurfa.2021.126573.

[61] S.N. Alam, N. Sharma, L. Kumar, Synthesis of Graphene Oxide (GO) by Modified Hummers Method and Its Thermal Reduction to Obtain Reduced Graphene Oxide (rGO)*, Graphene. 06 (2017) 1–18. https://doi.org/10.4236/graphene.2017.61001.

[62] M.J. Madito, M.Y.A. Ismail, T.T. Hlatshwayo, C.B. Mtshali, The nature of surface defects in Xe ion-implanted glassy carbon annealed at high temperatures: Raman spectroscopy analysis, Appl. Surf. Sci. 506 (2020) 145001. https://doi.org/10.1016/j.apsusc.2019.145001.

[63] S. Vollebregt, R. Ishihara, F.D. Tichelaar, Y. Hou, C.I.M. Beenakker, Influence of the growth temperature on the first and second-order Raman band ratios and widths of

carbon nanotubes and fibers, Carbon N. Y. 50 (2012) 3542–3554. https://doi.org/10.1016/j.carbon.2012.03.026.

[64] M.J. Matthews, M.A. Pimenta, G. Dresselhaus, M.S. Dresselhaus, M. Endo, Origin of dispersive effects of the Raman D band in carbon materials, Phys. Rev. B - Condens. Matter Mater. Phys. 59 (1999). https://doi.org/10.1103/physrevb.59.r6585.

[65] I. Pócsik, M. Hundhausen, M. Koós, L. Ley, Origin of the D peak in the Raman spectrum of microcrystalline graphite, J. Non. Cryst. Solids. 227–230 (1998) 1083–1086. https://doi.org/10.1016/S0022-3093(98)00349-4.

[66] A. Sadezky, H. Muckenhuber, H. Grothe, R. Niessner, U. Pöschl, Raman microspectroscopy of soot and related carbonaceous materials: Spectral analysis and structural information, Carbon N. Y. 43 (2005) 1731–1742. https://doi.org/10.1016/j.carbon.2005.02.018.

[67] A. Cuesta, P. Dhamelincourt, J. Laureyns, A. Martínez-Alonso, J.M.D. Tascón, Raman microprobe studies on carbon materials, Carbon N. Y. 32 (1994) 1523–1532. https://doi.org/10.1016/0008-6223(94)90148-1.

[68] B. Martín-García, M.M. Velázquez, F. Rossella, V. Bellani, E. Diez, J.L. García Fierro, J.A. Pérez-Hernández, J. Hernández-Toro, S. Claramunt, A. Cirera, Functionalization of Reduced Graphite Oxide Sheets with a Zwitterionic Surfactant, ChemPhysChem. 13 (2012) 3682–3690. https://doi.org/10.1002/cphc.201200501.

[69] A. Alkhouzaam, H. Qiblawey, M. Khraisheh, M. Atieh, M. Al-Ghouti, Synthesis of graphene oxides particle of high oxidation degree using a modified Hummers method, Ceram. Int. 46 (2020) 23997–24007. https://doi.org/10.1016/j.ceramint.2020.06.177.

[70] TUINSTRA F, KOENIG JL, Raman Spectrum of Graphite, J. Chem. Phys. 53 (1970) 1126–1130. https://doi.org/10.1063/1.1674108.

[71] O. Fasakin, J.K. Dangbegnon, D.Y. Momodu, M.J. Madito, K.O. Oyedotun, M.A. Eleruja, N. Manyala, Synthesis and characterization of porous carbon derived from activated banana peels with hierarchical porosity for improved electrochemical performance, Electrochim. Acta. 262 (2018) 187–196. https://doi.org/10.1016/j.electacta.2018.01.028.

[72] M.N. Rantho, M.J. Madito, N. Manyala, High-performance symmetric supercapacitor

device based on carbonized iron-polyaniline/nickel graphene foam, J. Alloys Compd. 819 (2020) 152993. https://doi.org/10.1016/j.jallcom.2019.152993.

[73] R. Kumar, S.K. Dhawan, H.K. Singh, A. Kaur, Charge transport mechanism of thermally reduced graphene oxide and their fabrication for high performance shield against electromagnetic pollution, Mater. Chem. Phys. 180 (2016) 413–421. https://doi.org/10.1016/j.matchemphys.2016.06.025.

[74] A. Eckmann, A. Felten, A. Mishchenko, L. Britnell, R. Krupke, K.S. Novoselov, C. Casiraghi, Probing the Nature of Defects in Graphene by Raman Spectroscopy, Nano Lett. 12 (2012) 3925. https://doi.org/10.1021/nl300901a.

[75] Y. He, J. Pan, L. Wu, Y. Zhu, X. Ge, J. Ran, Z.J. Yang, T. Xu, A novel methodology to synthesize highly conductive anion exchange membranes, Sci. Rep. 5 (2015). https://doi.org/10.1038/srep13417.

[76] P. Murovhi, D.J. Tarimo, K.O. Oyedotun, N. Manyala, High specific energy asymmetric supercapacitor based on alpha-manganese dioxide/activated expanded graphite composite and activated carbon-polyvinyl alcohol, J. Energy Storage. 32 (2020) 101797. https://doi.org/10.1016/j.est.2020.101797.

[77] A. Karaphun, C. Phrompet, W. Tuichai, N. Chanlek, C. Sriwong, C. Ruttanapun, The influence of annealing on a large specific surface area and enhancing electrochemical properties of reduced graphene oxide to improve the performance of the active electrode of supercapacitor devices, Mater. Sci. Eng. B. 264 (2021) 114941. https://doi.org/10.1016/J.MSEB.2020.114941.

[78] J.P. Diard, B. Le Gorrec, C. Montella, Linear diffusion impedance. General expression and applications, J. Electroanal. Chem. 471 (1999) 126–131. https://doi.org/10.1016/S0022-0728(99)00262-4.

[79] M. Mahdavian, M.M. Attar, Another approach in analysis of paint coatings with EIS measurement: Phase angle at high frequencies, Corros. Sci. 48 (2006) 4152–4157. https://doi.org/10.1016/j.corsci.2006.03.012.